

## Dual-TRACER: High resolution fMRI with constrained evolution reconstruction

Xuesong Li<sup>a</sup>, Xiaodong Ma<sup>a</sup>, Lyu Li<sup>a,b</sup>, Zhe Zhang<sup>a</sup>, Xue Zhang<sup>a</sup>, Yan Tong<sup>c</sup>, Lihong Wang<sup>d,e</sup>, Sen Song<sup>f</sup>, Hua Guo<sup>a,\*</sup>

<sup>a</sup> Center for Biomedical Imaging Research, Department of Biomedical Engineering, Tsinghua University, Beijing, China

<sup>b</sup> Philips Healthcare, Shanghai, China

<sup>c</sup> FMRI Centre, Nuffield Department of Clinical Neurosciences, John Radcliffe Hospital, Oxford OX3 9DU, UK

<sup>d</sup> Department of Psychiatry, University of Connecticut Health Center, Farmington, CT, USA

<sup>e</sup> Department of Psychiatry and Behavioral Science, Duke University, Durham, NC, USA

<sup>f</sup> Department of Biomedical Engineering, Tsinghua University, Beijing, China

### ARTICLE INFO

#### Keywords:

fMRI  
High resolution  
Variable density spiral  
TRACER  
Dual-TRACER

### ABSTRACT

fMRI with high spatial resolution is beneficial for studies in psychology and neuroscience, but is limited by various factors such as prolonged imaging time, low signal to noise ratio and scarcity of advanced facilities. Compressed Sensing (CS) based methods for accelerating fMRI data acquisition are promising. Other advanced algorithms like k-t FOCUSS or PICCS have been developed to improve performance. This study aims to investigate a new method, Dual-TRACER, based on Temporal Resolution Acceleration with Constrained Evolution Reconstruction (TRACER), for accelerating fMRI acquisitions using golden angle variable density spiral. Both numerical simulations and in vivo experiments at 3T were conducted to evaluate and characterize this method. Results show that Dual-TRACER can provide functional images with a high spatial resolution ( $1 \times 1 \text{ mm}^2$ ) under an acceleration factor of 20 while maintaining hemodynamic signals well. Compared with other investigated methods, dual-TRACER provides a better signal recovery, higher fMRI sensitivity and more reliable activation detection.

### Introduction

The conventional fMRI acquisition method, single-shot echo planar imaging (EPI), usually suffers from low spatial resolution and image distortion due to its low bandwidth along the phase-encoding direction, despite its fast imaging speed. It has been shown that improved spatial resolution can be beneficial to localize activation more accurately (Farivar et al., 2016; Feinberg and Yacoub, 2012; Hirose et al., 2013; Martuzzi et al., 2014; Suthana et al., 2015; Yacoub et al., 2003). Multi-shot EPI techniques (Cheng et al., 2001; Menon et al., 1997) can be used to improve the spatial resolution, but they prolong the imaging time and decrease the temporal resolution. Ultra-high magnetic field MRI such as 7 T systems can also be used to improve the image resolution; however, such systems are not widely available and cannot be used in clinical setting at present (Martuzzi et al., 2014; Ugurbil, 2012; Yacoub et al., 2008). Therefore, new fMRI techniques with high spatial resolution are desirable.

One typical solution to achieve high spatial resolution for fMRI is parallel imaging, which recovers image from under-sampled data by

using coil information. For example, SENSE (Preibisch et al., 2003; Pruessmann et al., 1999; Weiger et al., 2002) and GRAPPA (Griswold et al., 2002; Heidemann et al., 2006) have been used for fMRI acceleration. However, the acceleration factor of parallel imaging is usually limited, since it is restricted by the number of elements in phased array coils and the g-factor issue, which is the noise amplification during the reconstruction (Pruessmann et al., 1999). Therefore, parallel imaging alone has limited performance for improving fMRI resolution.

Compressed sensing (CS) is a particularly promising technique for fast MRI (Lustig et al., 2007, 2008). It can recover images under the sub-Nyquist sampling rate by enforcing sparsity in a certain transform domain, such as wavelet or total variation (TV). Incoherent aliasing artifacts from random sampling in CS also facilitate nonlinear reconstruction. CS combined with parallel imaging has been successfully used to improve spatial/temporal resolution or shorten the scan time in dynamic MR imaging, such as cardiac imaging (Otazo et al., 2014), liver imaging (Feng et al., 2014), and time-resolved angiography (Lee et al., 2013). CS has also been introduced to fMRI to accelerate signal

\* Corresponding author.

E-mail address: [huaguo@tsinghua.edu.cn](mailto:huaguo@tsinghua.edu.cn) (H. Guo).

acquisitions (Jeromin et al., 2012; Jung and Ye, 2009; Jung et al., 2007). In the study by Zong et al., CS accelerated GRE fMRI using Gaussian random sampling along the phase-encoding direction can achieve a reduction factor of 4 with a single channel coil (Zong et al., 2014). k-t FOCUSS was developed to accelerate fMRI acquisition based on shared temporal information (Jung et al., 2009). k-t FASTER, an approach based on low rank constraints of matrix completion, can achieve a reduction factor of 4.27 using k<sub>z</sub>-t pseudo-random Cartesian sampling (Chiew et al., 2015). Prior image constrained CS (PICCS) and TV-based CS were also developed to reconstruct highly under-sampled fMRI data (Chavarrías et al., 2015). With the advantage of the non-coherent acquisition for fMRI, variable density spiral (VDS) can be suitable for CS imaging (Holland et al., 2011, 2013). Recently, a high spatial resolution method was reported using VDS with a balanced steady state free precession sequence, which achieved a reduction factor of 5.3 with a single channel coil (Fang et al., 2016).

Other techniques for fast high resolution fMRI include view sharing with generalized series model (Nguyen and Glover, 2013), constrained reconstruction using low-rank spatiotemporal structure (Nguyen and Glover, 2014), and multiplexing (Feinberg et al., 2010). In addition, simultaneous multi-slice imaging (SMS) techniques (Larkman et al., 2001; Moeller et al., 2010) have also been introduced to fast fMRI, which can accelerate data acquisition by reducing the repetition time (TR) (Zahneisen et al., 2014). SMS can be combined with the in-plane acceleration methods to conduct fMRI with high spatial and temporal resolution.

Xu et al. proposed a time-resolved imaging technique for dynamic contrast-enhanced MRI, temporal resolution acceleration with constrained evolution reconstruction (TRACER), for liver lesion diagnosis. With signal acquisition by a stack of spirals, TRACER can provide three-dimensional volume coverage with a high temporal frame rate from highly under-sampled data. The image reconstruction in this method is based on the hypothesis that temporal changes are small at short time intervals (Xu et al., 2013).

In this study, we propose a new high resolution fMRI method, Dual-TRACER, based on TRACER, for accelerated acquisition using golden angle VDS. Dual-TRACER also assumes that signal change between adjacent frames is small. The image of the current frame is imposed to be similar to its neighboring frames. The constraint contributes to the recovery of fMRI images especially from highly undersampled data. Compared with the original method, Dual-TRACER reduces error accumulation by forward and backward operation. Both numerical simulations and in vivo experiments at 3T were conducted to evaluate the performance of Dual-TRACER. This new method was also compared with the original TRACER, PICCS, k-t FOCUSS and TV-based CS.

## Theory

### fMRI data formulation

In fMRI, the k-space data can be formulated as

$$y = PFSx \quad (1)$$

Where  $y$  is the k-space data,  $x$  is the image,  $S$  is the coil sensitivity map,  $F$  is the non-uniform Fast Fourier transform (NUFFT) (Fessler, 2007) operator and  $P$  is the k-space projection onto sampling trajectories. Starting with this basic equation, we can formulate models for advanced image reconstruction.

### Compressed sensing

Based on the theory of CS, the image can be recovered from highly under-sampled data, if certain sparse domain exists and a random sampling pattern is used. The CS reconstruction is formulated as follows:

$$\hat{x} = \arg \min \{ \|y - F(x)\|_2^2 + \lambda \|\psi x\|_1 \} \quad (2)$$

where  $x$  is a vector containing the images of all frames,  $\psi$  is a sparse transform operator,  $\lambda$  is the regularization weight and  $F = PFS$ . Random sampling can be achieved using either specially designed Cartesian trajectories or non-Cartesian trajectories such as radial or VDS. Different transforms can be used to form a sparse domain, including TV, wavelet transform and Fourier transform. In this study, we implemented CS with TV in both the spatial and temporal dimension, k-t FOCUSS and PICCS methods. For TV-based CS, the model is as follows:

$$\hat{x} = \arg \min \{ \|y - F(x)\|_2^2 + \lambda_t \|TV_t x\|_1 + \lambda_s \|TV_s x\|_1 \} \quad (3)$$

where  $TV_t$  and  $TV_s$  are TV operators along the temporal and spatial dimensions;  $\lambda_t$  and  $\lambda_s$  are regularization weights.

For the k-t FOCUSS method, time series are separated into spatial and time domain.

$$\Delta \hat{x} = \arg \min \{ \|y - F_s(x_0) - F_t F_s(W \Delta x)\|_2^2 + \lambda \|\Delta x\|_2^2 \}, \quad x = x_0 + F_t(W \Delta x) \quad (4)$$

where  $F_s$  is Fourier transform in the spatial domain,  $F_t$  is Fourier transform in the time domain and  $W$  is the weighting matrix which is updated in each iteration (Jung et al., 2009).

For the PICCS method, images are solved based on spatial TV of two items, TV of  $x$  and TV of  $x - x_{ref}$ , shown by the following equation:

$$\hat{x} = \arg \min \{ \|y - F(x)\|_2^2 + u \|x\|_1 + \lambda_r \|TV_s(x - x_{ref})\|_1 + \lambda_s \|TV_s(x)\|_1 \} \quad (5)$$

where  $\lambda_r$  and  $\lambda_s$  are regularization weights for the two TV items.

## TRACER

TRACER was originally developed for 3D liver dynamic imaging (Xu et al., 2013). Assuming that the change of signal intensity between adjacent frames is small, the  $n$ -th frame of reconstructed image  $x_n$  is forced to be close to the previous frame  $x_{n-1}$ . Using this constraint, TRACER can provide high spatiotemporal resolution images with a large undersampling rate. Using the iterative regularized Gauss-Newton method, the corresponding reconstruction is formulated as follows:

$$\hat{x}_n = \arg \min \{ \|y_n - F(x_{n,m})\|_2^2 + \lambda \|x_{n,m} - x_{n,0}\|_2^2 \}, \quad (6)$$

where  $m$  is the current iteration number. The fMRI image  $x_n$  can be reconstructed iteratively. The initial guess for the  $n$ -th frame  $x_{n,0}$  is set to the previous frame  $x_{n-1}$ . Since the sampling trajectory is rotated using a golden angle for different time frames, the initial value of the first frame  $x_0$  is set to the image reconstructed from the fully-sampled data combing the first  $N$  interleaves, where  $N$  is also the acceleration factor. The minimization problem of Eq. (6) is solved by a conjugate gradient algorithm.

Based on Eq. (6), TRACER enforces data fidelity to the under-sampled data of the current time frame, and maintains image quality by imposing consistency with the previous frame. The pseudocodes are listed in the Appendix A.

### Dual-TRACER

In TRACER, since the reconstruction of current frame depends on the previous frame, errors can be accumulated gradually along the time series. To suppress the error accumulation, we executed the reconstruction one more time by reversing the order of time series and setting  $x_{n,0} = x_{n+1}$ . The results from TRACER (or forward-TRACER) and backward-TRACER are then averaged to form the final images. The proposed method is therefore called Dual-TRACER.

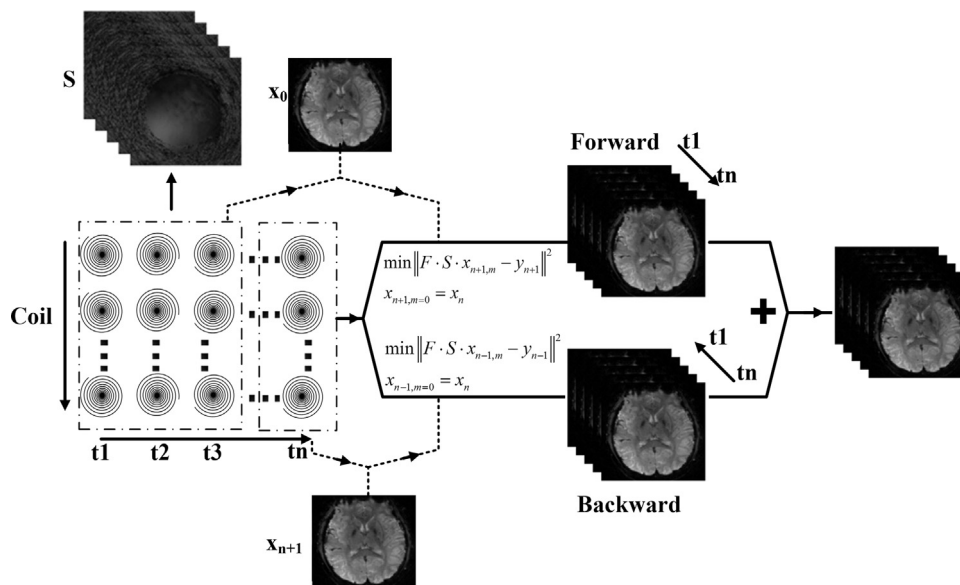


**Fig. 1.** The reconstruction flowchart of Dual-TRACER. Acquisitions along the coil and time series dimensions are shown. The reconstruction is executed in both forward and backward orders, and the final image is formed from the two calculations.

## Methods

Ten healthy subjects were scanned (7M and 3F, age 21–30 years, mean 26 years), following the approval by the Institutional Review Board at Tsinghua University with subjects' written informed consent. All data were collected on a 3T Philips Achieva scanner (Philips Healthcare, Best, The Netherlands) with a 32-channel head coil.

## Numerical simulation

Simulation was conducted to evaluate Dual-TRACER in comparison with four additional methods, TV-based CS, PICCS, k-t FOCUSS, and TRACER. Conventional single-shot EPI acquisition was used to obtain the reference fMRI images during a 4-min finger tapping task (20 s on and 20 s off). Other parameters included, TE=35 ms, TR=2 s, FOV=230×230 mm<sup>2</sup>, acquisition matrix=128×128. Coil sensitivity maps for a virtual eight-channel coil were computed using the Biot-Savart law analytically.

Using the acquired fMRI images as the “ground truth”, the under-sampled k-space data were generated via the following steps: (1) multiply the reference fMRI images by the sensitivity maps of different channels; transform the multi-channel images into full-sampled k-space with  $N$ -interleaf VDS trajectories ( $\alpha=4$ ) using NUFFT; (2) under-sample the k-space with different acceleration factors. To keep the temporal resolution the same as that of the single-shot EPI, we chose to use one interleaf for each frame. As a result, the acceleration factor is equal to the number of interleaves  $N$ . Between two adjacent frames, sampled trajectories were rotated by a golden angle to provide complementary information. In this study, acceleration factors from 4 to 28 were tested. The acquisition matrix size was set to 128×128.

## In vivo experiments

In vivo fMRI experiments were conducted using visual stimulus and finger tapping tasks. Prospectively under-sampling was used to acquire the hemodynamic data directly.

The golden angle rotated VDS ( $\alpha=4$ ) was used for data acquisition, which fulfills the requirement of incoherent aliasing artifacts for CS (Lustig et al., 2008), and helps remove aliasing artifacts for TRACER and Dual-TRACER. To control off-resonance induced blurring artifacts, which are amplified by a long readout duration of spiral sampling, the

acquisition windows were set between 17ms and 24ms in all experiments. Consequently, when a higher resolution is acquired, a larger number of interleaves are needed for the full-sampled k-space to meet the Nyquist sampling rate. In addition, only one interleave was used to sample each frame, following the sampling pattern in the simulation. Then for each time point, the acceleration factor was equal to the number of spiral interleaves  $N$ . PB-volume shimming provided by the Philips scanner was used in all functional acquisitions.

The stimulus paradigm to induce functional brain activation in the visual cortex was a 4-min block design consisting of 20 s of blank screen fixation alternating with 20 s of a flashing and rotating checkerboard at 8 Hz. The subjects were instructed to passively fixate on a cross-hair in the center of the video screen at all times. Two datasets with different spatial resolutions were acquired: 1.3×1.3 mm<sup>2</sup> with 8× acceleration, 1.0×1.0 mm<sup>2</sup> with 20× acceleration. Other imaging parameters included: FOV=200×200 mm<sup>2</sup> TR/TE=2000/35 ms. 30 slices were acquired with a slice thickness of 3 mm and a gap of 0 mm, above and below the Calcarine fissure. 120 time points were acquired to form a dynamic time course. One run was acquired for each testing scheme.

The finger tapping paradigm to induce functional brain activation in the motor cortex was a 4-min block design consisting of 20 s of rest alternating with 20 s of unilateral right finger tapping. For the fMRI data acquisition, the optimized scheme from the visual stimulus experiment was used, i.e. only the 1×1 mm<sup>2</sup> resolution with 20× acceleration was tested to validate the selected protocol from the former experiment. Other imaging parameters including TR, TE and FOV were the same as the visual stimulus experiment.

High-resolution T1-weighted structural images were acquired with slice thickness of 1 mm without a gap. Other imaging parameters were: TR/TE=9.5/4.5 ms, FOV=200×200×90 mm<sup>3</sup>, image resolution=0.8×0.8×1 mm<sup>3</sup>. 90 slices were acquired in 1.5 min.

## Optimization of regularization weights

The regularization weights were optimized through the simulation data by minimizing the root-mean-square error (RMSE) of the reconstructed images for TV-based CS, k-t FOCUSS, PICCS, and TRACER after a coarse parameter search. The acceleration factor is 4x. The calculation of RMSE is described in the Data Analysis section.

For PICCS, the range of  $\lambda_r$  and  $\lambda_s$  was investigated from 1e-1 to 1e-4 with 7 steps for the two TV items.

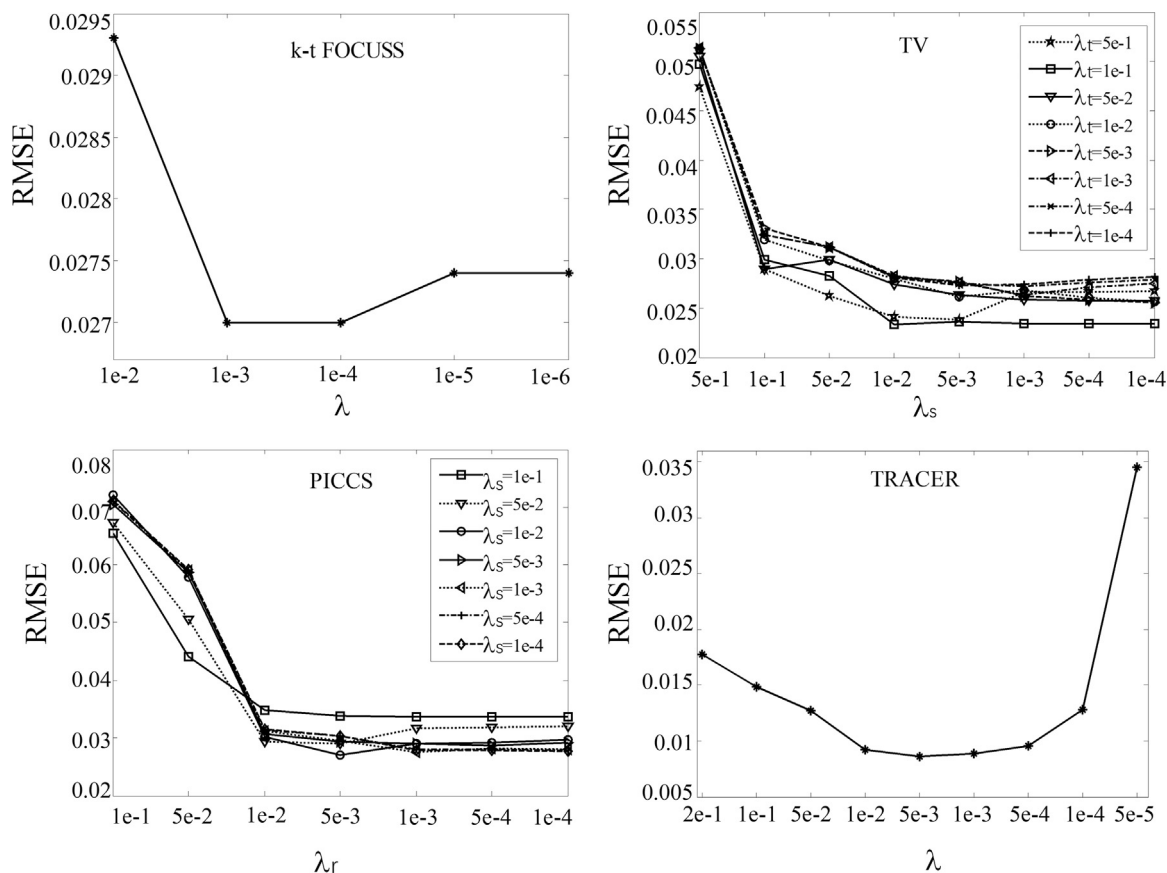


Fig. 2. Optimization of regularization weights for k-t FOCUSS, TV-based CS, PICCS and TRACER. The optimal values were chosen based on the minimal RMSE.

For TV-based CS, the range of  $\lambda_s$  and  $\lambda_t$  was investigated from  $5e-1$  to  $1e-4$  with 8 steps in both temporal and spatial dimensions.

For k-t FOCUSS, the range of  $\lambda$  was investigated from  $1e-2$  to  $1e-6$  with 5 steps.

For TRACER, the range of  $\lambda$  was investigated from  $2e-1$  to  $5e-5$  with 9 steps.

The k-space dataset was normalized to enable the regularization parameters not to change for different acceleration acquisitions.

Image reconstruction

Under-sampled VDS data were reconstructed with conventional reconstruction using NUFFT, TV-based CS, PICCS, k-t FOCUSS,

TRACER and Dual-TRACER. We used the approach of Lustig to solve Eqs. (3)–(5) (Lustig et al., 2007). An NUFFT algorithm (Fessler and Sutton, 2003) with Kaiser-Bessel kernel was utilized to grid the non-Cartesian data. For NUFFT, the oversampling ratio was 2 and the width of the convolving function was 8. A Voronoi weight function was utilized to compensate the sampling density of VDS in k-space domain. The optimized weights from the simulation were applied in the in vivo experiments.

The reconstruction flowchart of Dual-TRACER is shown in Fig. 1. Sensitivity maps were computed from the first group of the fully-sampled k-space data, which were the first  $N$  spiral interleaves. In the reconstruction, forward-TRACER and backward-TRACER were conducted separately, where the initial guess was set to the image

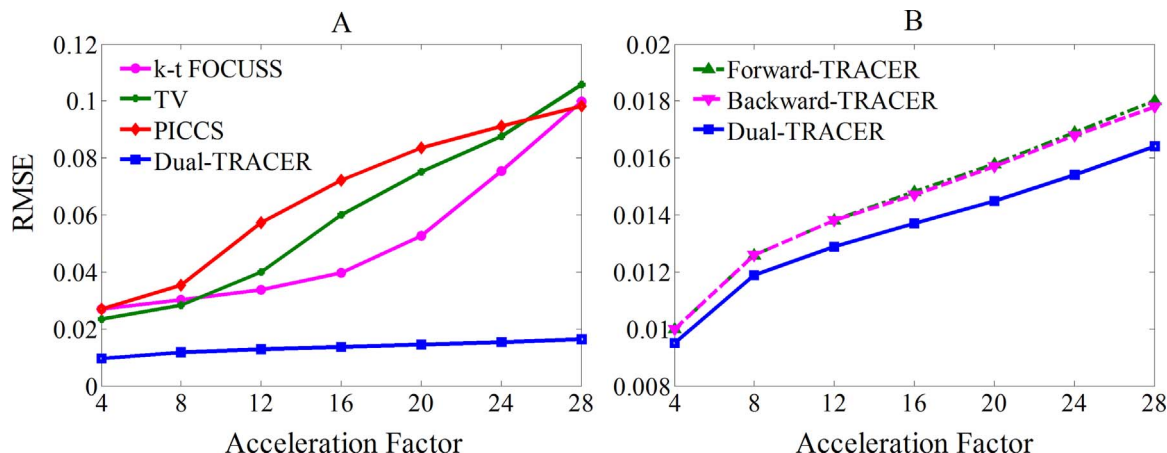
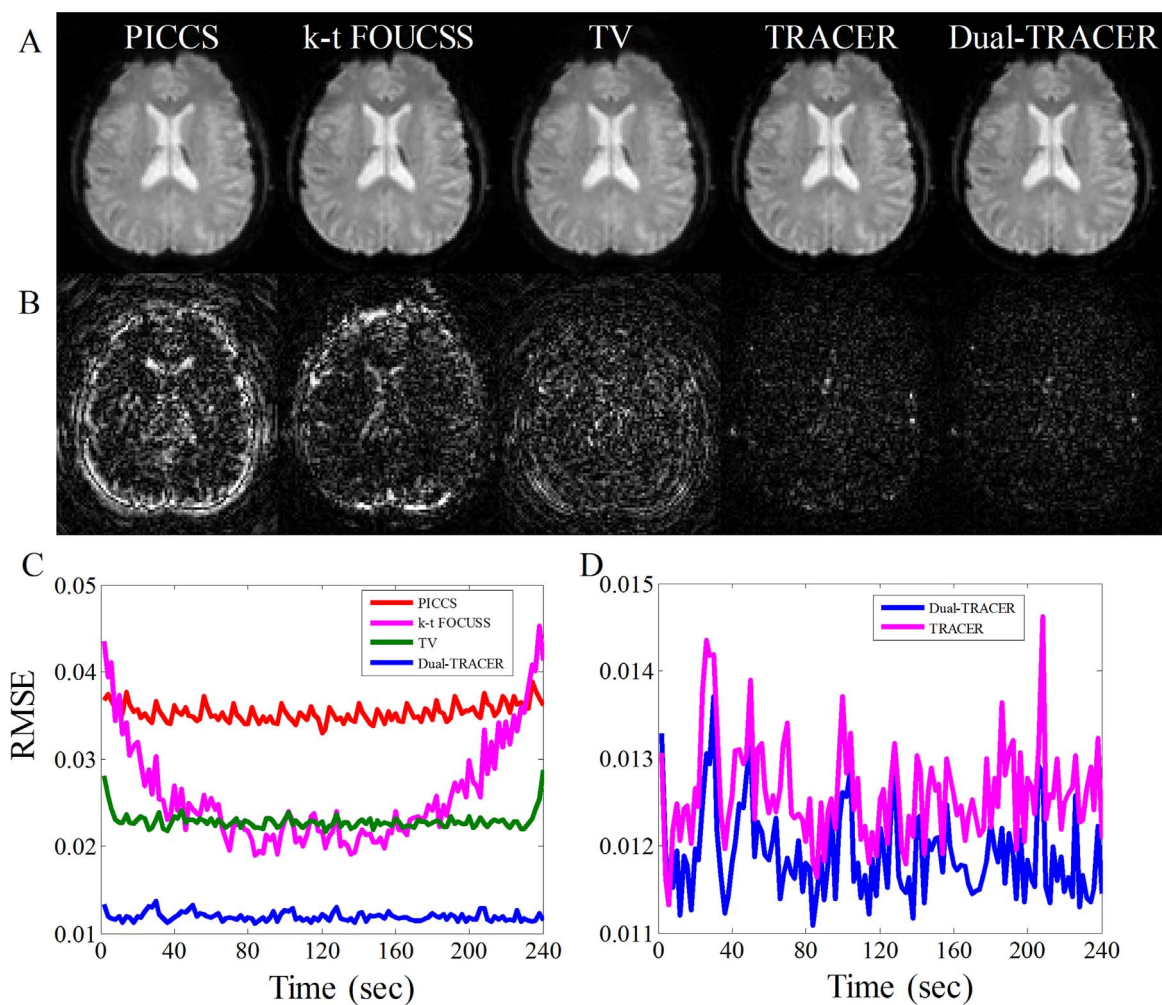


Fig. 3. RMSE comparison at different acceleration factors from 4 to 28 in simulation. (A) Comparison of Dual-TRACER, k-t FOCUSS, PICCS and TV-based CS. (B) Comparison of Dual-TRACER with forward-TRACER and backward-TRACER.



**Fig. 4.** The reconstructed images and RMSEs from different reconstruction methods, with an acceleration factor of 8. (A) The reconstructed image of one frame by each method. (B) Corresponding error maps amplified by a factor of 20. (C, D) RMSE values of reconstructed images of all frames by different methods. Note that the RMSE values of Dual-TRACER and TRACER are plotted in (D) because they cannot be distinguished in (C).

calculated from either the first or the last  $N$  frame, respectively. The maximum iteration number was 100 and the stopping criterion  $Tol$  was  $10^{-5}$  (Appendix A). The images obtained by the two procedures were then averaged to form the final images.

All the reconstruction procedures were implemented using Matlab (Mathworks Inc., Natick, MA) on a PC with 3.10 GHz quad-core CPU and 32 GB RAM.

#### Data analysis

fMRI pre-processing and statistical analysis were performed in FEAT V6.00 of FSL (Smith et al., 2004). Pre-processing steps included motion correction by MCFLIRT, high-pass temporal filtering ( $> 0.01$  Hz), and co-registration by self-developed MATLAB scripts. No smoothing was applied. Head motion was minor for all scans, in which translations were less than 1.5 mm and rotations were less than  $1^\circ$ . Pixel-wise activation maps were calculated using a general linear model (GLM) with a regressor specific for each task. A standard gamma neurovascular-coupling model as the hemodynamic response function was convolved with the blocks. Local autocorrelation correction (Woolrich et al., 2001) was then performed. The P values were corrected by using the familywise error (FWE) method with  $P_{FWE} < 0.05$  (Holland et al., 2013).

In order to evaluate the performance of different methods in the

simulation, two quantitative indices were calculated as follows.

Root-mean-square error (RMSE) is defined as follows:

$$RMSE = \frac{1}{N} \sum_{i=1:N} \frac{\|\hat{x}_i - x_i\|_F}{\|x_i\|_F} \quad (7)$$

where  $\hat{x}_i$  is the reconstructed image,  $x_i$  is the reference,  $i$  represents the index of frame, and  $N$  is the total number of frames.  $F$  is the Frobenius norm, i.e., the root of sum-of-square of all elements in one matrix.

Signal sensitivity (SEN) and false positive rate (FPR) are defined as follows:

$$SEN = \frac{TP}{FN + TP} \quad (8)$$

$$FPR = \frac{FP}{FP + TN} \quad (9)$$

where TP, FN, FP, TN are the numbers of true positive, false negative, false positive and true negative voxels, respectively, within the 5-pixel perimeter layers of the activation volume (Fang et al., 2016).

The degrees of freedom (DOF) were also computed to evaluate what benefit the accelerated reconstruction can provide (Krugel et al., 2002).

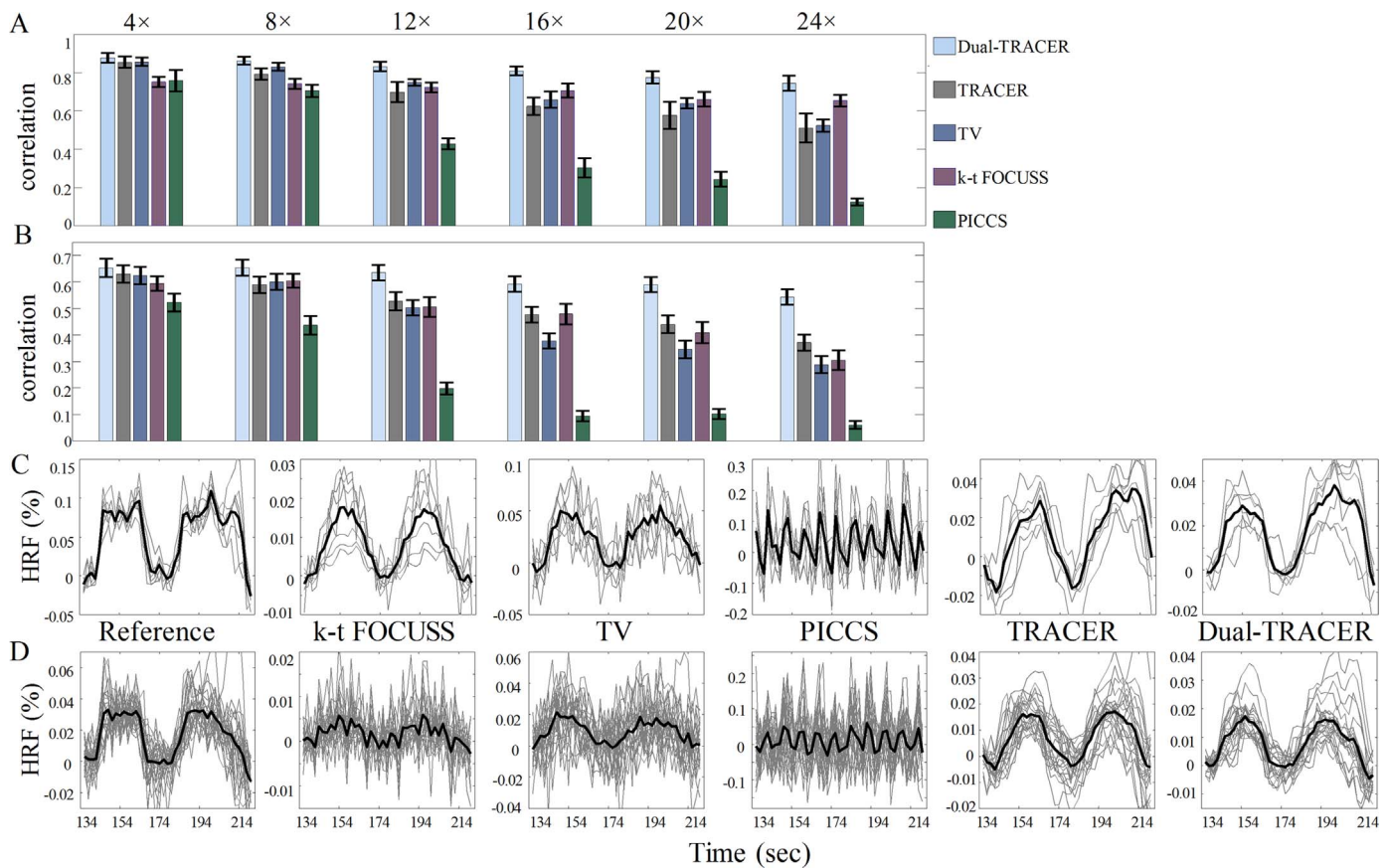


**Fig. 5.** Comparison of correlation (A, B) and dynamic signals (C, D) reconstructed by different methods at high and low peak HRF amplitudes. Five reconstruction methods are evaluated: Dual-TRACER, TRACER, TV-based CS, k-t FOCUSS, and PICCS. (A, B) Mean correlations for high and low peak HRF amplitudes, respectively. (C, D) Recovered signals at high and low peak HRF amplitudes, respectively, for an acceleration factor of 24. The gray lines in (C) and (D) denote signals from voxels with different amplitudes, and black lines denote the averaged signals.

**Results**

*Optimization of regularization weights*

As shown in Fig. 2, the optimal  $\lambda$  is  $1e-3$  for k-t FOCUSS;  $\lambda_t=1e-1$ ,  $\lambda_s=1e-2$  for TV-based CS;  $\lambda_r=5e-3$ , and  $\lambda_g=1e-2$  for PICCS;  $\lambda=5e-3$  for TRACER.

*Numerical simulation*

To evaluate the reconstruction performance of Dual-TRACER,

different acceleration factors from 4 to 28 were used, and the corresponding RMSE values were obtained using Eq. (7). As shown in Fig. 3A, Dual-TRACER provides smaller RMSE values than k-t FOCUSS, PICCS and TV. In addition, Dual-TRACER achieves better results than TRACER or backward-TRACER, shown in Fig. 3B, although the difference is smaller than that from other CS based methods. The reconstructed images of one frame (8x acceleration) and the corresponding error maps by different methods are shown in Fig. 4A and B, and the RMSE values of all frames are plotted in Fig. 4C and D. It can be observed that Dual-TRACER produces smaller errors than other methods.

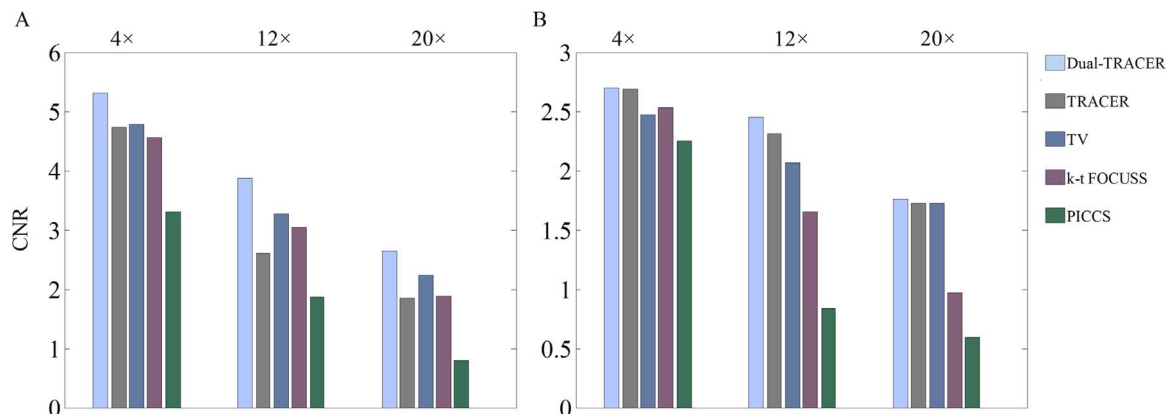


**Fig. 6.** Comparison of CNR reconstructed by different methods at high (A) and low (B) peak HRF amplitudes for different acceleration factors of 4, 12 and 20.

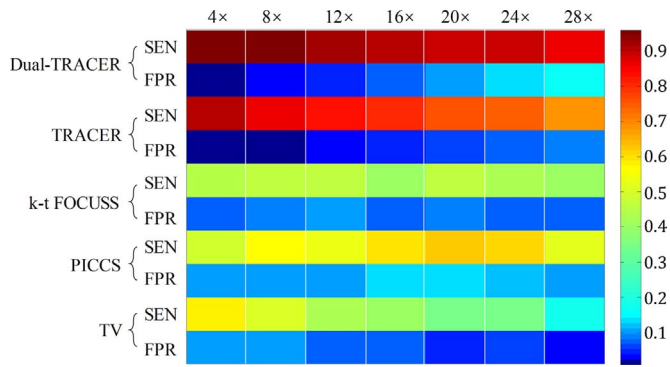


**Fig. 7.** SEN and FPR in Dual-TRACER, TRACER, k-t FOCUSS, PICCS and TV with undersampling factors from 4× to 28×.

In order to evaluate the performance of different methods at different contrast to noise ratio (CNR), the recovered dynamic signals at a high peak hemodynamic response function (HRF) amplitude (~8%) and a low peak HRF amplitude (~3%) are plotted in Fig. 5C and D, with an acceleration factor of 24 (Fang et al., 2016). Two representative periods are plotted. It is observed that k-t FOCUSS and TV-based CS can recover signals accurately at a high peak HRF amplitude, but cannot at a low value. TRACER and Dual-TRACER

worked well at both peak HFR amplitude, while PICCS failed at both amplitudes.

In order to quantitatively evaluate the recovered signals from different methods, averaged pixel-wise correlation between the hemodynamic signals and the reference for high and low peak HRF amplitudes were calculated and are shown in Fig. 5A and B, respectively. Acceleration factors from 4 to 24 were examined. Results show Dual-TRACER achieves a higher correlation with the reference than other methods, in both high and low peak HRF amplitudes, indicating that Dual-TRACER can recover signals more reliably. Other methods performed well for low acceleration factors under 8×. For high acceleration factors, TV-based CS and k-t FOCUSS worked well at the high peak HRF amplitude, but showed poor performance at the low levels.

The CNRs of the different reconstruction methods at both high and low peak HRF amplitudes are also compared in Fig. 6. Dual-TRACER has the highest CNR among the five methods.

In Fig. 7, SEN and FPR results generated by different reconstruction methods with undersampling factors from 4× to 28× are listed. Dual-TRACER and TRACER have higher SEN and FPR than other methods, and Dual-TRACER has the highest SEN. For the cost of the high SEN, there is a higher FPR in Dual-TRACER than TRACER, although they have a relative lower FPR than other methods with the undersampling factors from 4× to 12×. For higher undersampling factors (> 16×), it is difficult to detect activated regions for other CS based methods.

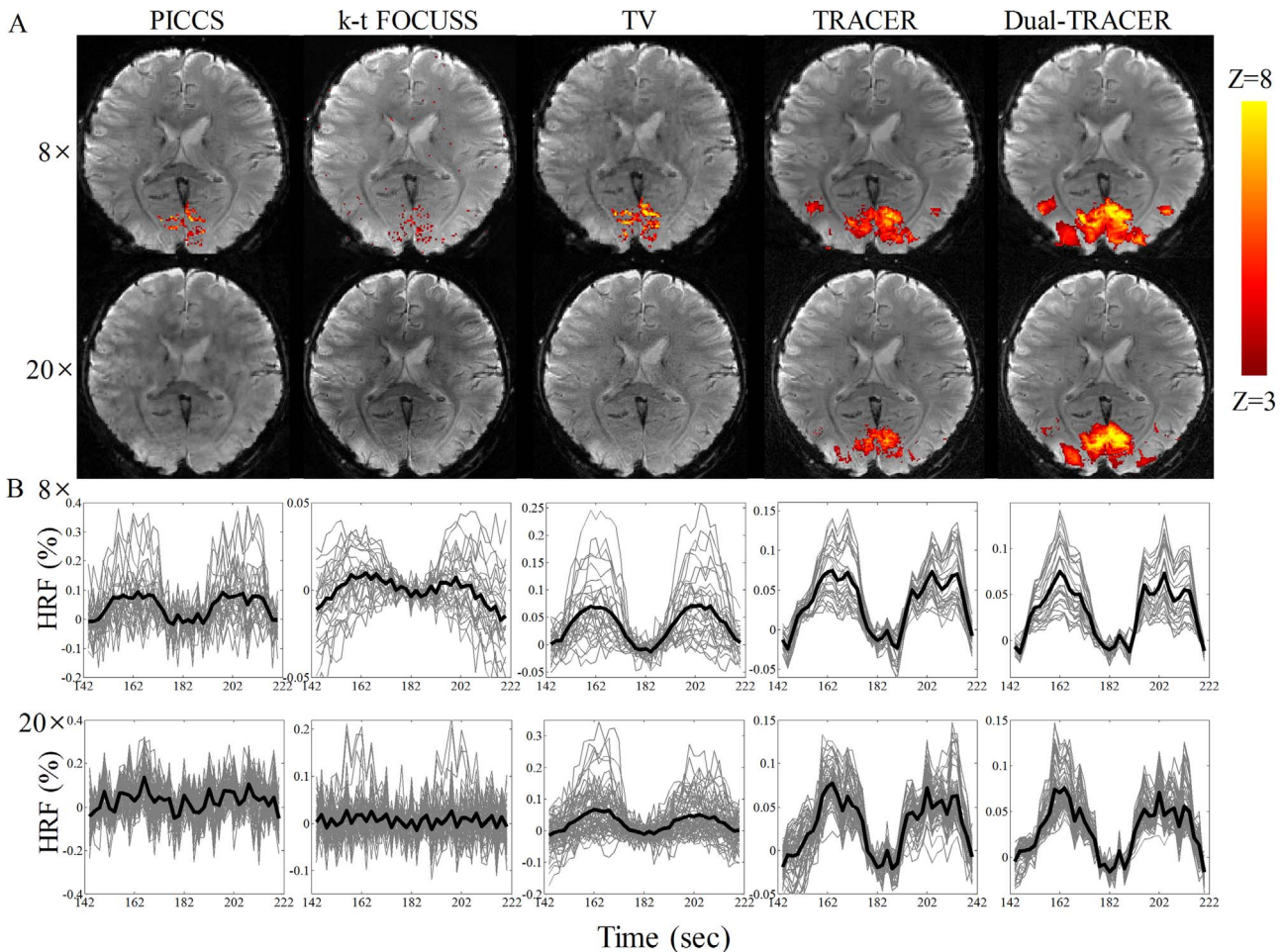


**Fig. 8.** Comparison of the activation maps and hemodynamic signals from PICCS, k-t FOCUSS, TV based CS, TRACER and Dual-TRACER in the visual stimulus experiment, at acceleration of 8 (resolution=1.3×1.3 mm<sup>2</sup>) and 20 (resolution=1×1 mm<sup>2</sup>). (A) The activation maps are overlaid onto fMRI images from different reconstruction methods. (B) The hemodynamic signals from different methods. The gray lines denote the signal from each voxel, and the black lines denote the averaged signal.

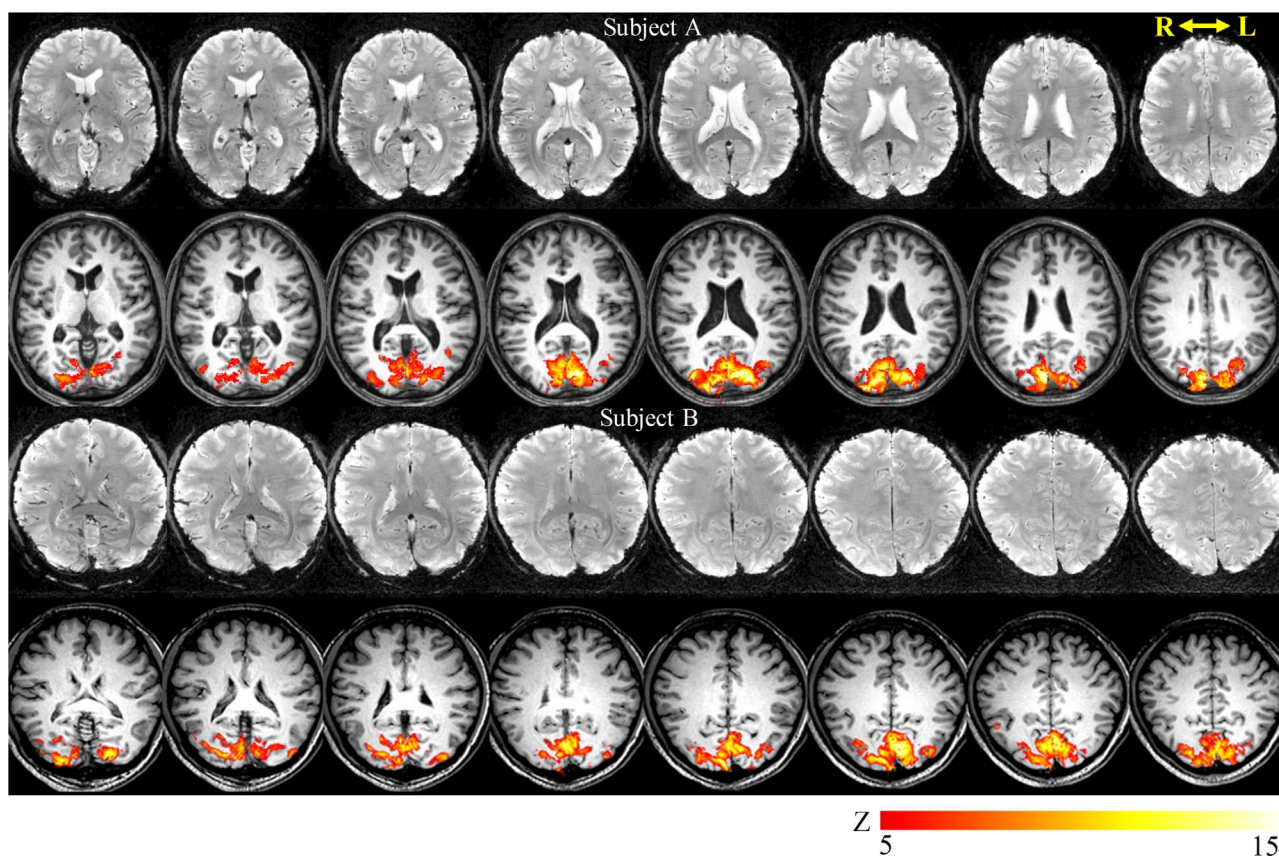


**Fig. 9.** Two more subjects from the visual stimulus experiment are presented. The acquisition used 20× under-sampling with a target resolution of  $1 \times 1 \text{ mm}^2$ . In the first row for each subject, functional images in different locations are shown. In the second row, activation maps are overlaid onto the T1 weighted images.

**Table 1**  
DOF for different reconstruction methods at different acceleration factors.

	4×	8×	12×	16×	20×	24×
Dual-TRACER	103	113	111	109	108	106
TRACER	112	108	104	97	98	98
TV	108	113	114	113	113	110
k-t FOCUSS	108	109	109	108	109	107
PICCS	94	115	116	115	113	113

### In vivo experiments

Fig. 8 shows the in vivo visual stimulus results using different reconstruction methods, for acceleration factors of 8 and 20. It is shown that for the same acceleration factor, Dual-TRACER and TRACER can provide more activated voxels than other methods based on CS, and are more capable of recovering time-series signals. TRACER has relatively weaker activation for the acceleration factor of 20, while Dual-TRACER has consistent performance for acceleration factors of 8 and 20.

The results by Dual-TRACER from another two subjects for the visual stimuli are shown in Fig. 9. The image resolution is  $1 \times 1 \text{ mm}^2$ , with an acceleration factor of 20. The visual cortex can be mapped by this method.

The DOF values for different reconstruction methods are shown in Table 1. For higher undersampling factors ( $\geq 8 \times$ ), DOF of Dual-TRACER is consistently larger than that of TRACER. When compared to TV based CS and PICSS, Dual-TRACER gives slightly lower DOF values.

The results of finger tapping experiment was shown in Fig. 10,

using 20× acceleration with a resolution of  $1 \times 1 \text{ mm}^2$ . Dual-TRACER can detect the activation more efficiently than PICCS, k-t FOCUSS, TV-based CS and TRACER.

### Discussion

In this study, a new reconstruction method, Dual-TRACER, is proposed for high-resolution fMRI. Simulations and in vivo experiments have demonstrated that the proposed method outperforms the tested CS-based methods and the original TRACER, by providing higher image quality and more accurate activation maps.

Although CS can recover images from under-sampled data for structural MRI, the acceleration factor for fMRI is limited. This is due to the inherently weak BOLD signals (Zong et al., 2014). In this study, the CS based methods can generate acceptable results at acceleration factors of 4–8 similar with previous studies (Chiew et al., 2015; Fang et al., 2016; Zong et al., 2014), but failed to provide reliable activation maps at larger factors.

As a novel fast imaging method in liver MRI, TRACER can generate high spatial and temporal resolution images from highly under-sampled data. It was later used for quantitative susceptibility mapping (QSM) to compute cerebral blood flow and cerebral blood volume, and showed a reliable performance (Xu et al., 2015). In TRACER, the image of the current frame is imposed to be similar to the previous frame, based on the assumption that the dynamic change of images is temporally smooth. This assumption is also used here for fMRI, by adopting an optimized scheme Dual-TRACER. Simulations and in vivo tests validate that Dual-TRACER is more advantageous than the CS-based methods and TRACER alone.

The temporal TV and the constraint in TRACER are similar since they both impose smoothness along the time dimension. However,

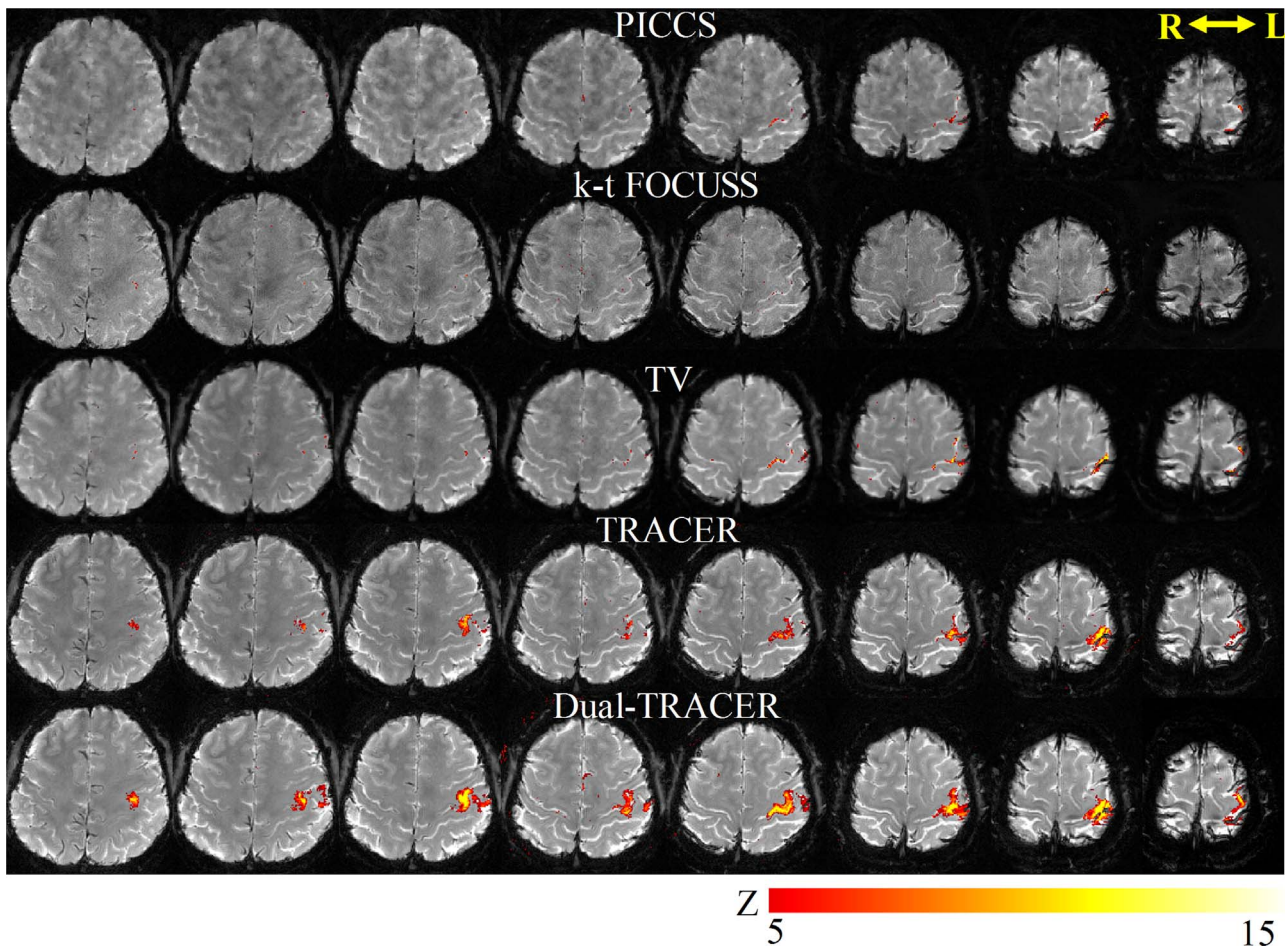


**Fig. 10.** Comparison of PICCS, k-t FOCUSS, TV-based CS, TRACER and Dual-TRACER in the finger tapping experiment. The acquisition used a 20× undersampling rate for a target resolution of  $1 \times 1 \text{ mm}^2$ .

instead of applying the directly enforced smoothness in temporal TV, TRACER utilizes the reconstructed image of the previous frame as the initialization for the current frame. After initialization, the current frame is not influenced by the previous frame. Therefore, the constraint in TRACER is considered to be a safer smoothing strategy than temporal TV. So the optimal RMSE for the TV method was larger than that of TRACER (Fig. 2).

For k-t FOCUSS, we chose the middle frames as the fully sampled frames, instead of the beginning and the end. Therefore, the middle frames had the lowest errors (Fig. 4). TV was computed by subtracting the current frame by its previous frame. For the first frame, since the previous frame did not exist, it was approximated by the current frame, which resulted in errors. And vice versa for the last frame it was processed similarly when inverse TV was conducted. That is why the TV method gave the largest RMSE on the edge (Fig. 4).

In simulation, Dual-TRACER can achieve accurate recovery with a small RMSE even with an acceleration factor of 28. In the in vivo experiment, however, there are various factors that could introduce artifacts such as off-resonance effects. In this study, an acceleration factor of 20 can be achieved with an in-plane resolution of  $1 \times 1 \text{ mm}^2$  in the brain. Both visual stimuli and finger tapping tests showed that Dual-TRACER can detect the activation maps reliably.

We tested different regularization factors for all acceleration factors used in this study, and found that the optimal factors are similar. The reason is that when different acceleration factors are used, only the spatial resolution is changed, whereas the temporal resolution remains identical. In other words, the frame-to-frame similarity is kept the same for different undersampling. Since the effective regularization is applied along the time dimension, the optimal lambda does not change

much theoretically. Therefore, we used a constant lambda for each method for simplicity.

Off-resonance artifacts can be a big issue for non-Cartesian sampling trajectory. High order shimming was used for the in vivo experiments. Additionally, the readout window of spiral acquisition was kept short and the blurring artifacts were not significant in the results. If longer readout windows are used or off-resonance effects are significant, blurring artifacts may need to be taken into consideration.

TRACER and Dual-TRACER are based on the assumption that fluctuation of the fMRI signals is small. In cases when the dynamic change between two adjacent frames is large, additional regularization terms are needed to take the large fluctuations into consideration. The reconstruction weights and performance of Dual-TRACER under these cases need further investigation in the future.

It is shown that the DOF of Dual-TRACER is larger than that of TRACER when the undersampling factor  $\geq 8 \times$  (Table 1). The reason can be that the accumulated errors in TRACER are reduced by forward and backward operations. The DOF values of Dual-TRACER are slightly lower than those of TV and PICCS, while they are comparable to k-t FOCUSS. This may need further investigation in the future.

In this study, although the in-plane fMRI spatial resolution can reach a sub-millimeter level with a common temporal resolution of 2 s, the through plane resolution, 3 mm, is clearly a limitation. Through-plane resolution can be improved using the super-resolution technique (Gholipour et al., 2010; Greenspan et al., 2002; Setsompop et al., 2015) and simultaneous multi-slice imaging (Larkman et al., 2001; Moeller et al., 2010). Three-dimensional golden angle spiral acquisition with Dual-TRACER reconstruction could potentially alleviate this issue as well (Xu et al., 2013).

## Conclusions

In this study, a new reconstruction method, Dual-TRACER, is proposed for high resolution fMRI from highly under-sampled data. Compared with the CS based methods and TRACER, Dual-TRACER

provides better signal fidelity, higher fMRI signal sensitivity and more reliable activation maps. The improved spatial resolution and maintained temporal resolution are potentially beneficial to psychiatry studies and neuroscience research.

## Appendix A

Iterative algorithm for the TRACER reconstruction.

---

```

 $f(x_n) = \|y_n - Ex_n\|^2 + \lambda \|x_n - x_{n,0}\|^2$ 
 $\nabla f(x_n) = (E^H E + \lambda)x_n - (\lambda x_{n,0} + E^H y_n)$ 
 $(E^H E + \lambda) = A \quad (\mu x_{n,0} + E^H y) = b$ 
% Initialization
tol = 1e-5, ite_max = 100;
n = 1
% Iterations
while (n ≤ frame_num)
  r_0 = b - Ax_{n,0}, p_0 = r_0
  k = 0
  while (k < ite_max or ||r_k|| > tol)
    α_k = (r_k^H r_k) / (p_k^H A p_k)
    x_{n,k+1} = x_{n,k} + α_k p_k
    r_{k+1} = r_k - α_k A p_k
    β_k = (r_{k+1}^H r_{k+1}) / (r_k^H r_k)
    p_{k+1} = r_{k+1} + β_k p_k
    k = k + 1
  end while
  x_n = x_{n,k-1}
  x_{n+1,0} = x_n
  n = n + 1
end while

```

---

## References

- Chavarrias, C., Abascal, J.F., Montesinos, P., Desco, M., 2015. Exploitation of temporal redundancy in compressed sensing reconstruction of fMRI studies with a prior-based algorithm (PICCS). *Med. Phys.* 42, 3814.
- Cheng, K., Waggoner, R.A., Tanaka, K., 2001. Human ocular dominance columns as revealed by high-field functional magnetic resonance imaging. *Neuron* 32, 359–374.
- Chiew, M., Smith, S.M., Koopmans, P.J., Graedel, N.N., Blumensath, T., Miller, K.L., 2015. k-t FASTER: acceleration of functional MRI data acquisition using low rank constraints. *Magn. Reson. Med.* 74, 353–364.
- Fang, Z., Van, Le, N., Choy, M., Lee, J.H., 2016. High spatial resolution compressed sensing (HSPARSE) functional MRI. *Magn. Reson. Med.* 76, 440–455.
- Farivar, R., Grigorenko, F., van der Kouwe, A.J., Wald, L.L., Keil, B., 2016. Dense, shape-optimized posterior 32-channel coil for submillimeter functional imaging of visual cortex at 3T. *Magn. Reson. Med.* 76, 321–328.
- Feinberg, D.A., Moeller, S., Smith, S.M., Auerbach, E., Ramanna, S., Gunther, M., Glasser, M.F., Miller, K.L., Ugurbil, K., Yacoub, E., 2010. Multiplexed echo planar imaging for sub-second whole brain fMRI and fast diffusion imaging. *PLoS One* 5, e15710.
- Feinberg, D.A., Yacoub, E., 2012. The rapid development of high speed, resolution and precision in fMRI. *Neuroimage* 62, 720–725.
- Feng, L., Grimm, R., Block, K.T., Chandarana, H., Kim, S., Xu, J., Axel, L., Sodickson, D.K., Otazo, R., 2014. Golden-angle radial sparse parallel MRI: combination of compressed sensing, parallel imaging, and golden-angle radial sampling for fast and flexible dynamic volumetric MRI. *Magn. Reson. Med.* 72, 707–717.
- Fessler, J.A., 2007. On NUFFT-based gridding for non-Cartesian MRI. *J. Magn. Reson.* 188, 191–195.
- Fessler, J.A., Sutton, B.P., 2003. Nonuniform fast Fourier transforms using min-max interpolation. *Signal Process.*, IEEE Trans. 51, 560–574.
- Gholipour, A., Estroff, J.A., Warfield, S.K., 2010. Robust super-resolution volume reconstruction from slice acquisitions: application to fetal brain MRI. *IEEE Trans. Med. Imaging* 29, 1739–1758.
- Greenspan, H., Oz, G., Kiryati, N., Peled, S., 2002. MRI inter-slice reconstruction using super-resolution. *Magn. Reson. Imaging* 20, 437–446.
- Griswold, M.A., Jakob, P.M., Heidemann, R.M., Nittka, M., Jellus, V., Wang, J., Kiefer, B., Haase, A., 2002. Generalized autocalibrating partially parallel acquisitions (GRAPPA). *Magn. Reson. Med.* 47, 1202–1210.
- Heidemann, R.M., Griswold, M.A., Seiberlich, N., Kruger, G., Kannengiesser, S.A., Kiefer, B., Wiggins, G., Wald, L.L., Jakob, P.M., 2006. Direct parallel image reconstructions for spiral trajectories using GRAPPA. *Magn. Reson. Med.* 56, 317–326.
- Hirose, S., Watanabe, T., Wada, H., Imai, Y., Machida, T., Shirouzu, I., Miyashita, Y., Konishi, S., 2013. Functional relevance of micromodules in the human association cortex delineated with high-resolution fMRI. *Cereb. Cortex* 23, 2863–2871.
- Holland, D.J., Liu, C., Bowen, C.V., Sederman, A., Gladden, L., Beyea, S.D., 2011. Highly Sparse Spiral fMRI Reconstructed with Compressed Sensing: Trajectory Optimization for BOLD Contrast. In: *Proceedings of the 19th Annual Meeting of ISMRM, Montreal, Canada*, p. 3591.
- Holland, D.J., Liu, C., Song, X., Mazerolle, E.L., Stevens, M.T., Sederman, A.J., Gladden, L.F., D'Arcy, R.C., Bowen, C.V., Beyea, S.D., 2013. Compressed sensing reconstruction improves sensitivity of variable density spiral fMRI. *Magn. Reson. Med.* 70, 1634–1643.
- Jeromin, O., Pattichis, M.S., Calhoun, V.D., 2012. Optimal compressed sensing reconstructions of fMRI using 2D deterministic and stochastic sampling geometries. *Biomed. Eng. Online* 11, 25.
- Jung, H., Sung, K., Nayak, K.S., Kim, E.Y., Ye, J.C., 2009. k-t FOCUS: a general compressed sensing framework for high resolution dynamic MRI. *Magn. Reson. Med.* 61, 103–116.
- Jung, H., Ye, J.C., 2009. Performance Evaluation of Accelerated Functional MRI Acquisition Using Compressed Sensing. 2009 IEEE International Symposium on Biomedical Imaging: From Nano to Macro, Vol. 1 and 2, pp. 702–705.
- Jung, H., Ye, J.C., Kim, E.Y., 2007. Improved k-t BLAST and k-t SENSE using FOCUS. *Phys. Med. Biol.* 52, 3201–3226.
- Kruggel, F., Pelegrini-Issac, M., Benali, H., 2002. Estimating the effective degrees of freedom in univariate multiple regression analysis. *Med. Image Anal.* 6, 63–75.
- Larkman, D.J., Hajnal, J.V., Herlihy, A.H., Coutts, G.A., Young, I.R., Ehnholm, G., 2001. Use of multicoil arrays for separation of signal from multiple slices simultaneously excited. *J. Magn. Reson. Imaging* 13, 313–317.
- Lee, G.R., Seiberlich, N., Sunshine, J.L., Carroll, T.J., Griswold, M.A., 2013. Rapid time-resolved magnetic resonance angiography via a multiecho radial trajectory and GraDeS reconstruction. *Magn. Reson. Med.* 69, 346–359.
- Lustig, M., Donoho, D., Pauly, J.M., 2007. Sparse MRI: the application of compressed

- sensing for rapid MR imaging. *Magn. Reson. Med.* 58, 1182–1195.
- Lustig, M., Donoho, D.L., Santos, J.M., Pauly, J.M., 2008. Compressed sensing MRI. *IEEE Signal Process. Mag.* 25, 72–82.
- Martuzzi, R., van der Zwaag, W., Farthouat, J., Gruetter, R., Blanke, O., 2014. Human finger somatotopy in areas 3b, 1, and 2: a 7T fMRI study using a natural stimulus. *Hum. Brain Mapp.* 35, 213–226.
- Menon, R.S., Thomas, C.G., Gati, J.S., 1997. Investigation of BOLD contrast in fMRI using multi-shot EPI. *NMR Biomed.* 10, 179–182.
- Moeller, S., Yacoub, E., Olman, C.A., Auerbach, E., Strupp, J., Harel, N., Ugurbil, K., 2010. Multiband multislice GE-EPI at 7 T, with 16-fold acceleration using partial parallel imaging with application to high spatial and temporal whole-brain fMRI. *Magn. Reson. Med.* 63, 1144–1153.
- Nguyen, H., Glover, G., 2014. Field-corrected imaging for sparsely-sampled fMRI by exploiting low-rank spatiotemporal structure. In: *Proceedings of the 22th Annual Meeting of ISMRM, Milan, Italy*, p. 0327.
- Nguyen, H.M., Glover, G.H., 2013. A modified generalized series approach: application to sparsely sampled fMRI. *IEEE Trans. Biomed. Eng.* 60, 2867–2877.
- Otazo, R., Candes, E., Sodickson, D.K., 2014. Low-rank plus sparse matrix decomposition for accelerated dynamic MRI with separation of background and dynamic components. *Magn. Reson. Med.*
- Preibisch, C., Pilatus, U., Bunke, J., Hoogenraad, F., Zanella, F., Lanfermann, H., 2003. Functional MRI using sensitivity-encoded echo planar imaging (SENSE-EPI). *Neuroimage* 19, 412–421.
- Pruessmann, K.P., Weiger, M., Scheidegger, M.B., Boesiger, P., 1999. SENSE: sensitivity encoding for fast MRI. *Magn. Reson. Med.* 42, 952–962.
- Setsompop, K., Bilgic, B., Nummenmaa, A., Fan, Q., Cauley, S.F., Huang, S., Chatnuntawech, I., Rathi, Y., Witzel, T., Wald, L.L., 2015. SLICE dithered enhanced resolution simultaneous multiSlice (SLIDER-SMS) for high resolution (700  $\mu$ m) diffusion imaging of the human brain. *ISMRM*, 339.
- Smith, S.M., Jenkinson, M., Woolrich, M.W., Beckmann, C.F., Behrens, T.E.J., Johansen-Berg, H., Bannister, P.R., De Luca, M., Drobnjak, I., Flitney, D.E., Niaz, R.K., Saunders, J., Vickers, J., Zhang, Y.Y., De Stefano, N., Brady, J.M., Matthews, P.M., 2004. Advances in functional and structural MR image analysis and implementation as FSL. *Neuroimage* 23, S208–S219.
- Suthana, N.A., Donix, M., Wozny, D.R., Bazih, A., Jones, M., Heidemann, R.M., Trampel, R., Ekstrom, A.D., Scharf, M., Knowlton, B., Turner, R., Bookheimer, S.Y., 2015. High-resolution 7T fMRI of human hippocampal subfields during associative learning. *J. Cogn. Neurosci.* 27, 1194–1206.
- Ugurbil, K., 2012. The road to functional imaging and ultrahigh fields. *Neuroimage* 62, 726–735.
- Weiger, M., Pruessmann, K.P., Osterbauer, R., Bornert, P., Boesiger, P., Jezzard, P., 2002. Sensitivity-encoded single-shot spiral imaging for reduced susceptibility artifacts in BOLD fMRI. *Magn. Reson. Med.* 48, 860–866.
- Woolrich, M.W., Ripley, B.D., Brady, M., Smith, S.M., 2001. Temporal autocorrelation in univariate linear modeling of FMRI data. *Neuroimage* 14, 1370–1386.
- Xu, B., Spincemaille, P., Chen, G., Agrawal, M., Nguyen, T.D., Prince, M.R., Wang, Y., 2013. Fast 3D contrast enhanced MRI of the liver using temporal resolution acceleration with constrained evolution reconstruction. *Magn. Reson. Med.* 69, 370–381.
- Xu, B., Spincemaille, P., Liu, T., Prince, M.R., Dutruel, S., Gupta, A., Thimmappa, N.D., Wang, Y., 2015. Quantification of cerebral perfusion using dynamic quantitative susceptibility mapping. *Magn. Reson. Med.* 73, 1540–1548.
- Yacoub, E., Duong, T.Q., Van De Moortele, P.F., Lindquist, M., Adriany, G., Kim, S.G., Ugurbil, K., Hu, X., 2003. Spin-echo fMRI in humans using high spatial resolutions and high magnetic fields. *Magn. Reson. Med.* 49, 655–664.
- Yacoub, E., Harel, N., Ugurbil, K., 2008. High-field fMRI unveils orientation columns in humans. *Proc. Natl. Acad. Sci. USA* 105, 10607–10612.
- Zahneisen, B., Poser, B.A., Ernst, T., Stenger, A.V., 2014. Simultaneous Multi-Slice fMRI using spiral trajectories. *Neuroimage* 92, 8–18.
- Zong, X.P., Lee, J.Y., Poplawsky, A.J., Kim, S.G., Ye, J.C., 2014. Compressed sensing fMRI using gradient-recalled echo and EPI sequences. *Neuroimage* 92, 312–321.